Journal of Materials Research and Technology 31 (2024) 47–61

Contents lists available at ScienceDirect

Journal of Materials Research and Technology

journal homepage: www.elsevier.com/locate/jmrt

Mapping the microstructure and the mechanical performance of a combinatorial Co–Cr–Cu–Fe–Ni–Zn high-entropy alloy thin film processed by magnetron sputtering technique

Péter Nagy [a], Maria Wątroba [b], Zoltán Hegedűs [c], Johann Michler [b], László Pethö [b], Jakob Schwiedrzik [b], Zsolt Czigány [d], Jenő Gubicza [a,*]

[a] Department of Materials Physics, ELTE Eötvös Loránd University, P.O. Box 32, H-1518, Budapest, Hungary
[b] EMPA Swiss Federal Laboratories for Materials Science and Technology, Laboratory for Mechanics of Materials and Nanostructures, Feuerwerkerstrasse 39, CH-3602, Thun, Switzerland
[c] Deutsches Elektronen-Synchrotron DESY, 22607, Hamburg, Germany
[d] Institute for Technical Physics and Materials Science, HUN-REN Centre for Energy Research, 1121, Budapest, Konkoly-Thege Miklós út 39-33, Hungary

ARTICLE INFO

Handling editor:SN Monteiro

Keywords:
High-entropy alloy
Magnetron sputtering
Thin film
Microstructure
Hardness

ABSTRACT

The Co–Cr–Cu–Fe–Ni–Zn compositional library was studied on a combinatorial high-entropy alloy thin film processed on a silicon substrate by magnetron sputtering technique. The thickness of the coating was between 2 and 3 μm while the lateral dimension was 10 cm. The chemical composition in the layer depended on the location and for each constituent element the concentration varied between 5 and 42 at.%. The phase composition and the microstructure were mapped using synchrotron X-ray diffraction, and the crystallite size as well as the density of lattice defects (dislocations and twin faults) were determined by diffraction line profile profile analysis. In addition, selected locations were studied by transmission electron microscopy. The influence of the chemical composition on the microstructure and the mechanical behavior was revealed. The mechanical performance was characterized by nanoindentation mapping which determined the hardness and the elastic modulus versus the element concentrations. It was found that the coating contains single phase face-centered cubic (FCC) and body-centered cubic (BCC) regions as well as an intermediate two-phase area. In the whole combinatorial sample, the microstructure consisted of nanocrystalline columns growing perpendicular to the coating surface and having pores between them. Due to the porosity, the hardness and the elastic modulus were relatively low despite the nanostructure and the very high defect density. The highest hardness (3.4 GPa) and elastic modulus (119 GPa) were measured in the BCC region with the chemical composition of 10%Co–38%Cr–13%Cu–27%Fe–5%Ni–7%Zn (at.%).

1. Introduction

In recent years, multi-principal element alloys (MPEAs) have drawn much attention due to the unique properties of many novel compositions. MPEAs represent a set of materials with three or more principal elements with similar concentrations [1,2]. Many MPEA compositions have a single-phase structure due to the stabilizing effect of the increased configuration entropy. When the configuration entropy of an MPEA surpasses the value of 1.61*R*, where *R* is the universal gas constant, the alloy is called high-entropy alloy (HEA) [3]. This threshold of the configuration entropy is achieved when an equimolar MPEA contains five or more elements [3]. There are HEA compositions exhibiting an enhanced strength combined with a good ductility which induced a great interest in these materials [4].

MPEA and HEA materials in the form of coatings and thin layers are also at the forefront of materials science owing to their potential applications in surface functionalization and mechanical strengthening [5–7]. Thin HEA layers have been manufactured via direct current magnetron sputtering [8,9], thermal evaporation [10], cold spraying [11], radio frequency sputtering [12] and multibeam sputtering [13]. Changing the conditions of the fabrication processes can influence the microstructure and chemical composition of MPEAs [12]. Fine tuning of the chemical composition can be used to optimize the mechanical and functional properties of the material [14].

* Corresponding author.
E-mail address: jeno.gubicza@ttk.elte.hu (J. Gubicza).

https://doi.org/10.1016/j.jmrt.2024.06.059
Received 25 April 2024; Received in revised form 25 May 2024; Accepted 9 June 2024
Available online 10 June 2024

Combinatorial samples represent the most effective way to study the effect of the chemical composition on the microstructure and mechanical properties for MPEA systems. Multicomponent alloys with one or more well-defined elemental gradients are called combinatorial samples which can be processed in both bulk and layer forms [15]. These materials contain a library of compositions of the principal elements, providing valuable research assets since it allows the investigation of the effect of the concentrations of the constitutive elements on the structure and properties of alloys [16]. Combinatorial thin film samples have been successfully produced by plasma solid-state surface metallurgy [17], magnetron sputtering [18], plasma sputtering [19] and multibeam sputtering [20,21]. Combinatorial MPEA samples were successfully used for the exploration of the composition dependence of the microstructure and the mechanical properties of Co–Cr–Fe–Ni combinatorial layer [20,21]. It was found that while most of the sample has a single-phase face-centered cubic (FCC) structure, the hardest location was found at the composition of 42% Co – 45% Cr– 5% Fe – 8% Ni (at. %), where the major phase was hexagonal closed-packed (HCP) [21]. The magnetic behaviour of the Al–Co–Cr–Fe–Mn system was also investigated as a function of the Al content [19]. It was found that this system achieved its maximum saturation magnetization at 8 at% Al concentration [19]. The effectiveness of the combinatorial samples in the study of MPEA libraries was also demonstrated on the Co–Cr–Fe–Mn–Ni system [22]. It was found that the FCC structure was stable in the vicinity of the equimolar CoCrFeMnNi composition (Cantor alloy).

In our former works, a combinatorial Co–Cr–Fe–Ni MPEA thin layer sample was processed by multibeam sputtering and the correlation between chemical and phase composition, microstructure, and mechanical properties were studied [20,21]. Our aim was to increase the number of constituent elements in the previously investigated quaternary system and the element selection was based on the literature. For instance, in the case of a $Fe_{40-X}Mn_{20}Co_{20}Cr_{15}Si_5Cu_X$ MPEA the addition of 1.5 at. % Cu increased the stability of the γ-FCC phase, and yielded a higher-strength without compromising the ductility [23]. In recent studies, the addition of different elements to Al–Cu–Fe–Si-X (X = Cr, Mn, Zn, Sn) system was investigated [24,25]. It was found that the addition of Zn resulted in a good elongation and energy absorption value [25]. Thus, based on the literature the addition of Cu and Zn to the formerly investigated Co–Cr–Fe–Ni system is expected to influence the phase composition and mechanical properties of the layer considerably. Therefore the present work aims to investigate a six-component Co–Cr–Cu–Fe–Ni–Zn thin film system and map the influence of the chemical composition on the phase content, microstructure and mechanical performance. The coating was deposited by Physical Vapor Deposition (PVD) onto the surface of a Si wafer with the diameter of 10 cm. The concentration of each element varies between 5 and 42 at%. Synchrotron radiation was used to map the phase composition, and the resulting patters were used to determine microstructural parameters by X-ray line profile analysis (XLPA). The microstructure is additionally characterized by transmission electron microscopy (TEM). The mechanical performance is mapped by nanoindentation, and the correlation between the structural parameters and the mechanical behavior is discussed in detail.

2. Methods

2.1. Processing of the combinatorial sample by magnetron sputtering

A Hex-L hexagonal chamber (manufacturer: Korvus Technology Ltd, High Wycombe, UK) was used for the synthesis of the six-component combinatorial Co–Cr–Cu–Fe–Ni–Zn film in a sputter-up arrangement. Two inch magnetrons were mounted on each sidepanel, 60° apart. Each target was a 50 mm diameter disk, with a purity above 99.95%, supplied by HMW-Hauner GmbH. The paramagnetic and ferromagnetic targets were 3 mm and 1 mm thick, respectively. The substrate was a Si single crystal with a diameter of 10 cm and a texture <100>. The substrate holder was stationary during deposition to get a combinatorial sample.

The base pressure obtained before deposition start was 8×10^{-7} mbar. For running the process, the chamber was fed with 40 sccm argon and the flow was evenly distributed among the magnetrons. The synthesis ran for a duration of 1 h, at 10^{-2} mbar process pressure and at room temperature. Table 1 summarizes the plasma parameters for each target material. The magnetrons were supplied by TDK Lambda DC sources in current control mode.

Deposition rate characterizations were carried out individually for each element, resulting in the determination of a current setpoint value for the magnetrons. Plasma parameters were chosen to obtain the equimolar point of the deposited thin film at the center of the substrate, which is also the confocal point of the magnetron arrangement. During the actual process deposition, the coexistence of six plasmas influences the obtained elemental distributions – the spatial overlap of the sputtering plume shapes and equilibration of voltages of neighbouring plasmas produce insignificant variations in the obtained elemental composition ranges of the synthesized film.

2.2. Mapping the chemical composition

The distribution of the constituent elements was investigated by X-ray fluorescence (XRF) spectroscopy (spectrometer type: FISCHERSCOPE X-RAY XDV-SDD, manufacturer: Helmut Fischer GmbH). The X-ray source was a microfocus tube with a tungsten anode. The detector was a Peltier-cooled Silicon Drift Detector (SDD). The composition was investigated in 360 spots in 9 concentric circles with different radii. The smallest circle had a radius of 5 mm. Two neighbouring circles had a 5 mm difference in their radii. Every circle included 40 measuring points, and the polar angular difference between two neighbouring points was 9°. Each examined spot had a diameter of 1 mm. The XRF data were also used for the determination of the thickness of the coating versus its composition.

2.3. Determination of the phase and microstructure maps

The investigation of the microstructure was conducted by synchrotron XRD. The measurement was carried out at the Deutsches Elektronen-Synchrotron (DESY), in Hamburg, Germany. The beam energy was 55 keV, corresponding to the X-ray wavelength of $\lambda = 0.023843$ nm. The measurement points were placed in a grid with 2 mm spacing in both horizontal and vertical directions denoted by axes X and Z, respectively. The XRD patterns were recorded in a horizontal range of $X = -50$ to 50 mm and a vertical range between $Z = 0$ and 88 mm, resulting in $45 \times 51 = 2951$ measurement points. The in-depth characterization of the microstructure was performed in 32 selected locations, but all the measurement data were utilized for the creation of the phase map of the sample. The dimensions of the X-ray spot on the sample surface in directions X and Z were 1.5 and 1 mm, respectively. The angle between the incident beam and the sample was 3.84°.

In the selected 32 positions, the diffractograms were also evaluated by X-ray line profile analysis (XLPA) in order to determine the parameters of the microstructure [26]. XLPA was performed using the Convolutional multiple whole profile (CMWP) fitting method [27]. In this procedure, all peak profiles in the experimental XRD pattern are fitted

Table 1
Plasma parameters for each target material used during deposition.

Target material	Feed current [mA]	Plasma potential [V]	Power consumed [W]
Cr	70	306	21.4
Fe	75	287	21.5
Co	65	252	16.4
Ni	70	273	19.1
Zn	35	523	18.3
Cu	40	340	13.6

simultaneously by the convolution of the theoretical intensity profiles broadened due to the small crystallite size, dislocations and twin faults. These three profile functions can be found in Ref. [26]. CMWP fitting yielded the area-weighted mean crystallite size, the dislocation density and the twin fault probability. The twin fault probability was determined only for the FCC phase where this quantity gives the fraction of the faulted {111} planes. In the theoretical intensity function related to dislocations, the dislocation density is multiplied with the square of the magnitude of the Burgers vector and the dislocation contrast factor for reflection with the indices *200* [26]. Therefore, for obtaining the dislocation density from CMWP fitting the values of the latter two parameters should be determined. For the BCC and FCC phases, the magnitudes of the Burgers vector were calculated as the product of the lattice constant and the factors of 0.866 and 0.707, respectively. The dislocation contrast factor value of reflection *200* depends on the single crystal elastic constants, i.e., it may vary as a function of the chemical composition in the studied MPEA disk. However, it has been shown in Ref. [26] that there is only a slight difference between the contrast factor values of the XRD peak *200* determined for very different cubic metals. Therefore, for the whole combinatorial disk a consistent value of 0.33 was used for the contrast factor of reflection *200* as obtained formerly for both edge and screw dislocations in FCC CoCrFeNi MPEA [28]. Instrumental correction was not utilized in the CMWP evaluation of the peak profiles since their breadth was much higher than the instrumental broadening. The lattice parameter of the main phase in these selected 32 points was determined from the XRD patterns using the Nelson-Riley method [29].

The microstructure was further investigated by TEM. The TEM specimens were cut from the coating by a focused ion beam (FIB). The FIB lamellae were lifted out and thinned using a Thermo Scientific Scios 2 Dual Beam equipment. The final steps in FIB preparation were made at 2 kV. The bright field (BF), dark field (DF) and selected area electron diffraction (SAED) TEM investigations as well as the high angle annular dark field scanning transmission electron microscopy (STEM-HAADF) and energy-dispersive X-ray spectroscopy (EDS) experiments were performed in a Cs corrected Themis (Thermo Fischer) microscope operated at 200 kV with 0.8 Å resolution.

2.4. Nanoindentation

The mechanical properties of the sample were characterized by nanoindentation. The measurements were performed using ex-situ scanning nanoindenter setup built in-house (Alemnis AG) equipped with a Berkovich diamond tip (Synton MDP). A matrix of 3 × 3 indents was performed in selected locations on the wafer. A maximum load of 2 mN was chosen to avoid any effect of the substrate on the mechanical properties. The maximum displacement was around 250 nm, which is less than 10% of the studied thin film thickness. The load-displacement data was analyzed using AMMDA software (Alemnis). For the determination of the hardness and the elastic modulus from the indentation curves, the Oliver–Pharr method was utilized [30].

3. Results

3.1. Compositional and phase mapping of the combinatorial sample

Fig. 1 shows the concentration distribution maps of the six constituent elements for the studied combinatorial Co–Cr–Cu–Fe–Ni–Zn coating as determined by XRF. The concentrations of Co, Cr, Cu, Fe, Ni and Zn vary in the ranges of 5–31%, 7–42%, 7–36%, 5–36%, 5–30% and 7–41% (at%), respectively. The map of the layer thickness values obtained by XRF is shown in Fig. 2. The thickness of the coating varied between 1960 and 2830 nm, and the highest value was obtained close to the Zn target.

Fig. 3 illustrates the map of the crystalline phases as obtained by XRD performed in 2951 points on the combinatorial disk surface. Single phase FCC and BCC regions as well as an intermediate two-phase area were identified. The single phase FCC and body-centered cubic (BCC) regions formed close to the targets Fe/Cr/Cu and Co/Ni/Zn, respectively. Very close to the Zn target a minor BCC phase also appeared beside the main FCC structure. The lattice constant of the BCC phase varied between 0.2862 and 0.2889 nm. For the FCC phase, the lattice

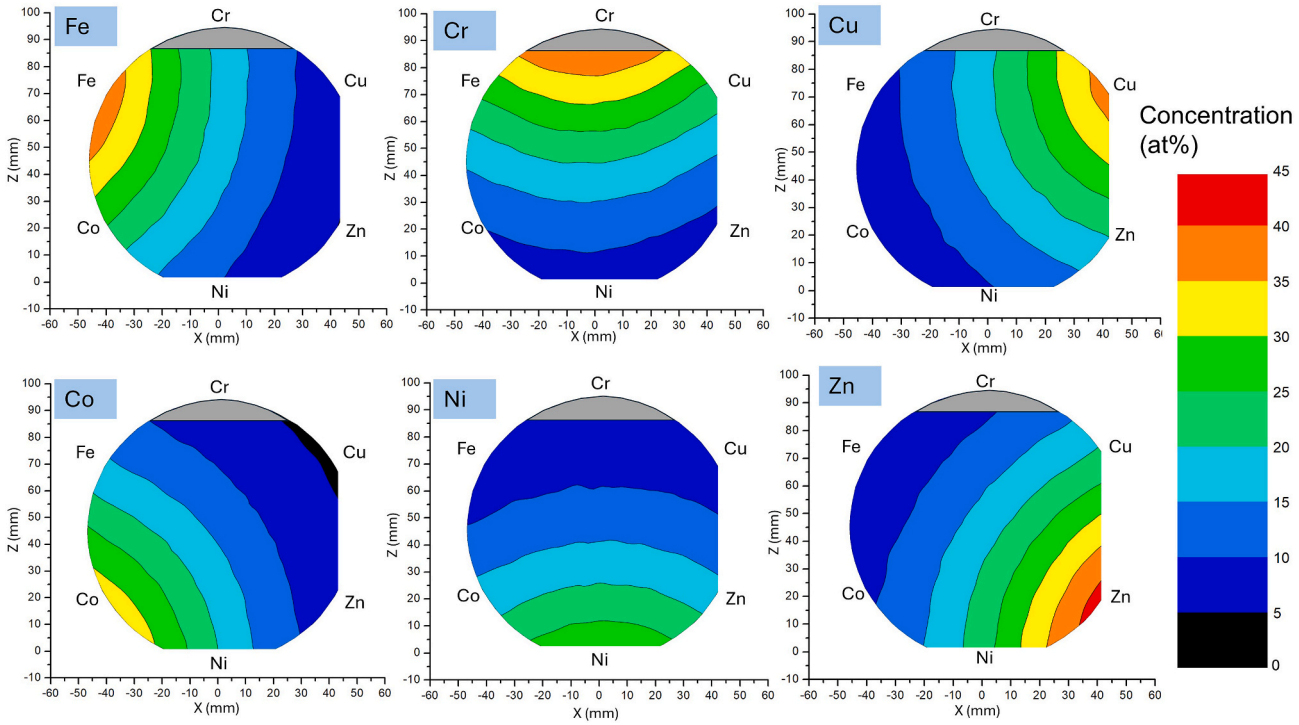

Fig. 1. Concentration distribution maps of the constituent elements determined by XRF for the combinatorial Co–Cr–Cu–Fe–Ni–Zn coating. The chemical symbols around the maps mark the approximate positions of the targets in PVD processing. The grey area near the Cr target was covered during the process.

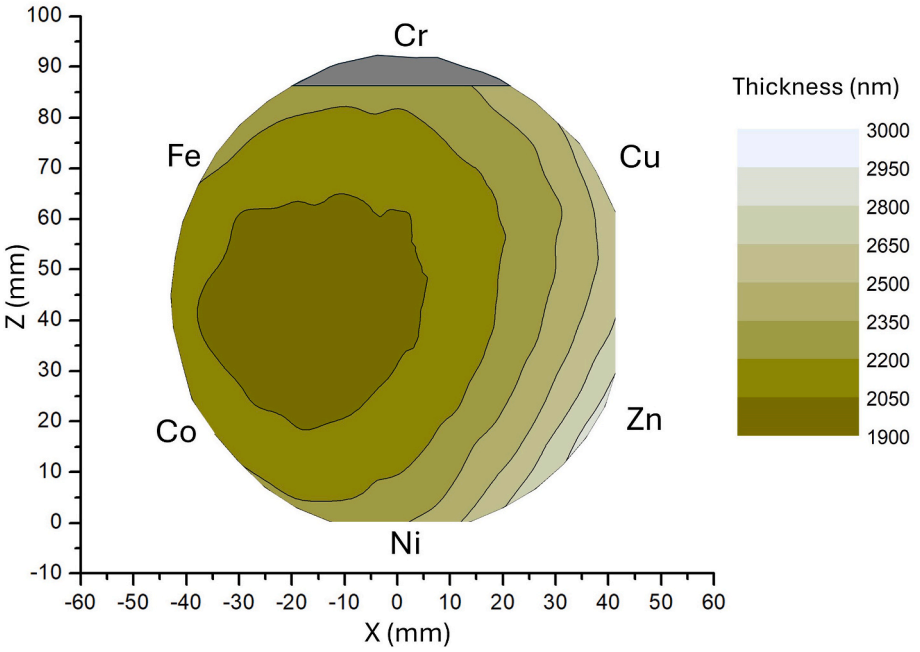

Fig. 2. Map of the layer thickness values obtained by XRF for the combinatorial Co–Cr–Cu–Fe–Ni–Zn coating. The chemical symbols around the map mark the approximate positions of the targets in PVD processing.

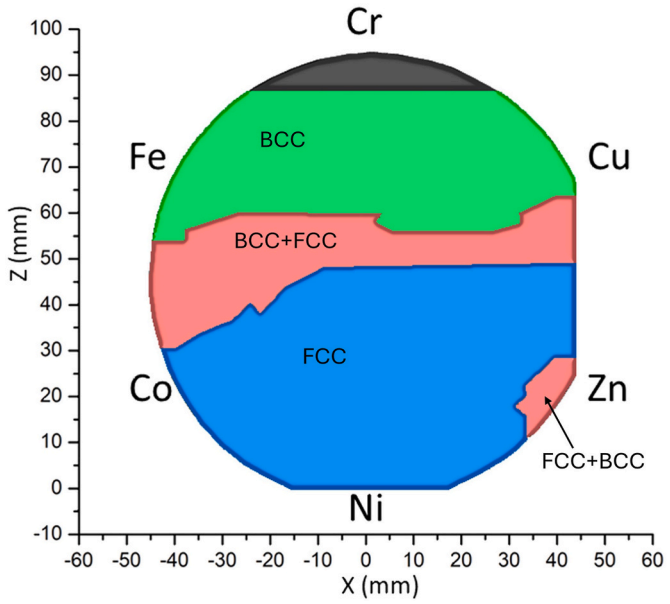

Fig. 3. Schematic representation of the map of the phases formed in the coating. In the case of two-phase regions, the first phase mentioned denotes the primary phase. The notations of the constituent elements around the disk represent the approximate position of the targets used during deposition. The grey area was covered during deposition.

parameter was between 0.3592 and 0.3656 nm. The lattice constant values for both phases are shown in Fig. 4. In the two-phase regions, the lattice constant of the main phase is plotted in the map. It should be noted that the lattice parameter values were determined experimentally only in those points where the XLPA study of the microstructure was also performed. These 32 locations distributed uniformly on the coating surface and are shown by white spots in Fig. 4. In the other points, the lattice constant was obtained by interpolation and extrapolation using the Origin software (Supplier: OriginLab Co., Northampton, USA). Thus, values out of the experimentally determined range can also be seen at the perimeter of the disk in Fig. 4. Nevertheless, it is evident that for both BCC and FCC phases the lattice constant increases in the direction of Cu and Zn targets, respectively, which can be explained by the relatively large atomic radii of these elements as discussed in section 4.

3.2. *Influence of chemical composition on mechanical behavior and microstructural parameters*

Fig. 5a and b shows the maps of hardness and elastic modulus as determined by nanoindentation. The black spots indicate those 32 points where the indentation was performed. The concentrations of the six constituent elements in these points are listed in Table S1 of the Supplementary materials. These points are the same as those where the XLPA evaluation of the microstructure and the lattice constant determination were carried out. The hardness and Young's modulus values obtained in the 32 points are listed in Table S2 of the Supplementary materials. Using the experimental hardness and modulus values obtained in the studied 32 points, the maps were created by interpolation and extrapolation using the Origin software. The highest hardness and elastic modulus with the values of 3.4 and 119 GPa, respectively, were observed in the BCC region at the disk perimeter between the Fe and Cr targets (see Fig. 5). The chemical composition at this location is 10% Co–38%Cr–13%Cu–27%Fe–5%Ni–7%Zn (at%). The lowest hardness (1.1 GPa) and modulus (63 GPa) were also detected in the BCC area with the composition of 7%Co–27%Cr–30%Cu–11%Fe–8%Ni–18%Zn (at%). Typical load-depth curves obtained by nanoindentation in these two points are shown in Fig. S1 of the Supplementary materials. In the FCC region, only slight differences in the mechanical behavior were observed. Namely, the hardness and the elastic modulus varied between 1.5-2.5 and 73–88 GPa, respectively.

The parameters of the microstructure were determined by XLPA using the CMWP fitting method. The studied 32 locations were the same as those used for the determination of the lattice constants and the mechanical properties. Since next to the Cu target the XRD pattern was very noisy, XLPA evaluation was performed only in 31 points. As examples, Fig. 6 shows fitted XRD patterns for the single-phase BCC and FCC regions as well as the two-phase area. In the latter case, only the peaks of the main phase were fitted (for the example shown in Fig. 6b,

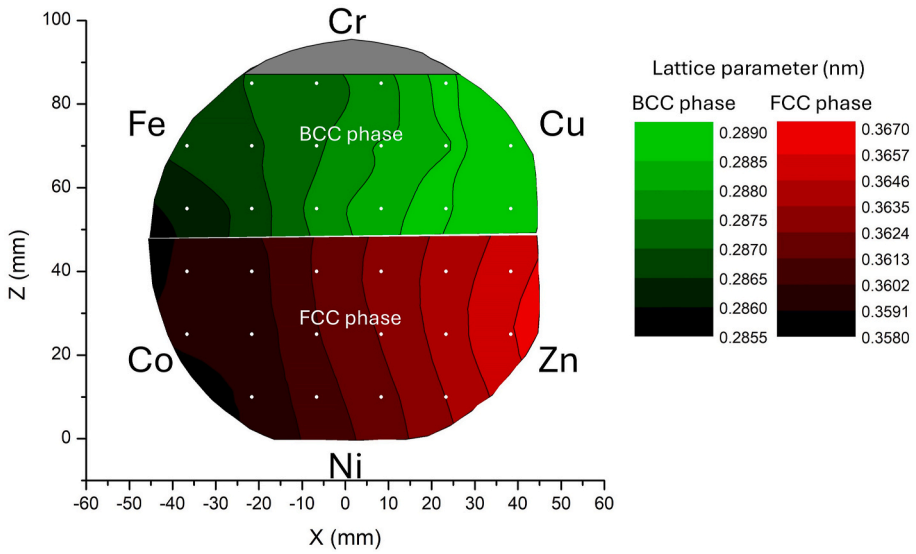

Fig. 4. Map of the lattice parameters of the main phases in the coating. The notations of the constituent elements around the disk represent the approximate position of the targets used during deposition. The locations of lattice parameter measurements performed by XRD are shown by white spots. For the two-phase regions identified in Fig. 3, only the lattice constant of the primary phase is shown in this map. Above and below the horizontal line, the BCC and FCC structures, respectively, are the main phases.

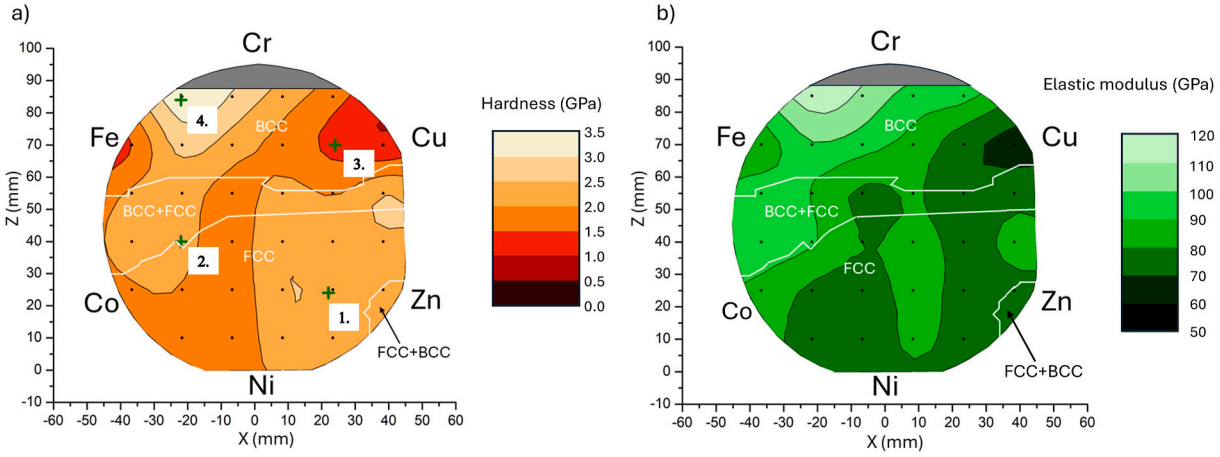

Fig. 5. a) Hardness and b) elastic modulus maps obtained by nanoindentation. The white curves indicate the boundaries of the regions with different phase contents. On the hardness map, the green crosses mark the positions of the TEM investigations which were numbered from 1 to 4 (shown in the white squares). The black spots indicate those 32 points where the indentation was performed. (For interpretation of the references to colour in this figure legend, the reader is referred to the Web version of this article.)

the BCC reflections). The microstructural parameters determined in the 31 points by XLPA are listed in Table S2 of the Supplementary materials. Figs. 7 and 8 present the maps for the crystallite size and the dislocation density for all regions with different phase contents. It is evident that the whole combinatorial sample is nanostructured with the crystallite size ranging between 10 and 30 nm. In the BCC and FCC phases, the crystallite size values vary between 20-30 and 10–20 nm, respectively. This suggests a finer nanostructure in the FCC phase. The dislocation density values were in the range of 70-270 $\times$ 10^{14} m^{-2} if the whole coating is considered. In the single phase BCC and FCC areas, the dislocation density values vary between 70 and 190 $\times$ 10^{14} m^{-2} and 110-270 $\times$ 10^{14} m^{-2}, respectively. It seems that the highest dislocation density values (above 200 $\times$ 10^{14} m^{-2}) can be found mainly in the FCC region. The twin fault probability map is shown only for the single-phase FCC region in Fig. 9 since twinning is less probable in the BCC phase. The twin fault probability values varied between 0.4 and 4.3%. The highest values were detected at the coating perimeter between the Ni and Zn targets.

Complementary TEM investigations of the microstructure were carried out in four selected points of the coating. The locations of these points are indicated by green crosses in Fig. 5a. Point No. 1 is in the single-phase FCC region where the hardness is relatively high. In location No. 2, an additional secondary BCC phase was observed beside the FCC matrix. Points No. 3 and No. 4 have the lowest and highest hardness values in the BCC phase, respectively.

Fig. 10 shows TEM images taken at the position No. 1. The film thickness was about 2.5 μm as revealed by the BF-TEM cross-sectional micrograph in Fig. 10a. This value is in good agreement with the thickness obtained by the XRF technique (see Fig. 2). TEM diffraction pattern indicated a single phase FCC structure in accordance with XRD result. In addition, the diffraction pattern obtained in TEM indicated an <111> preferred orientation perpendicular to the layer. In Fig. 10, the blue arrows indicate pores in the form of long channels aligned perpendicular to the film (i.e., parallel to the growth direction) which are typical morphology patterns caused by the direct current magnetron sputtering technique. There are channels which propagate through the

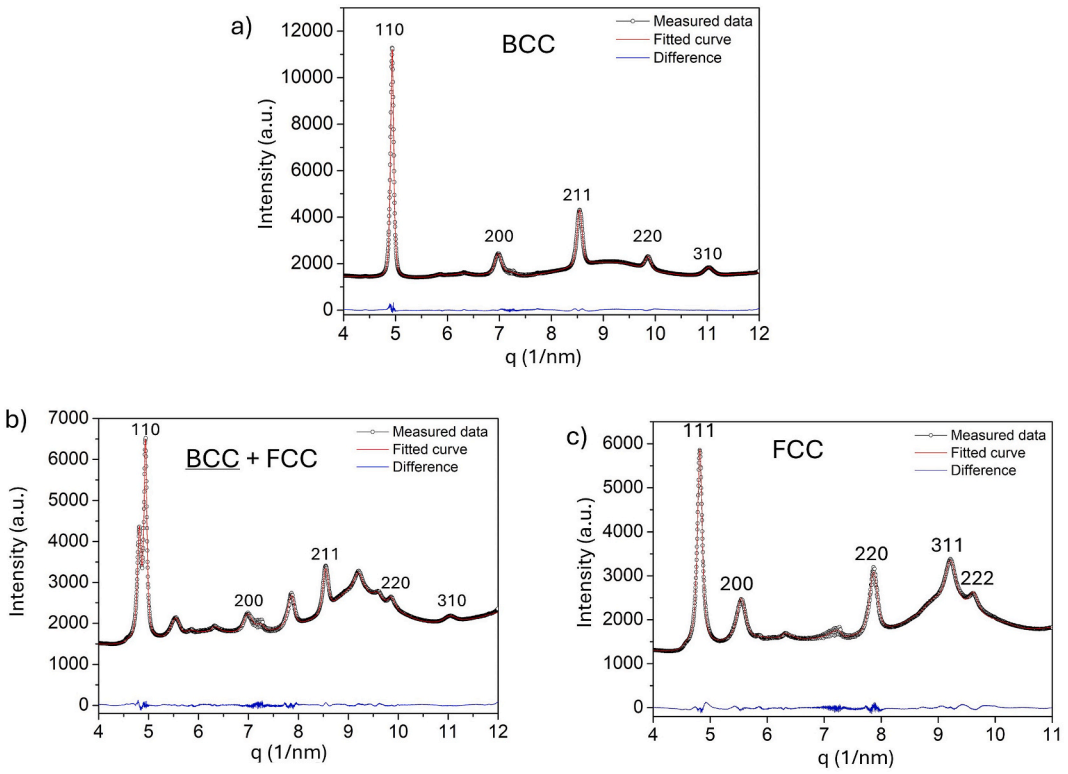

Fig. 6. CMWP fitting of the diffraction patterns taken at locations with a) BCC, b) two-phase BCC + FCC and c) FCC structures. In (b), only the peaks of the main BCC phase were fitted, and the reflections of the FCC phase were handled as a part of the background.

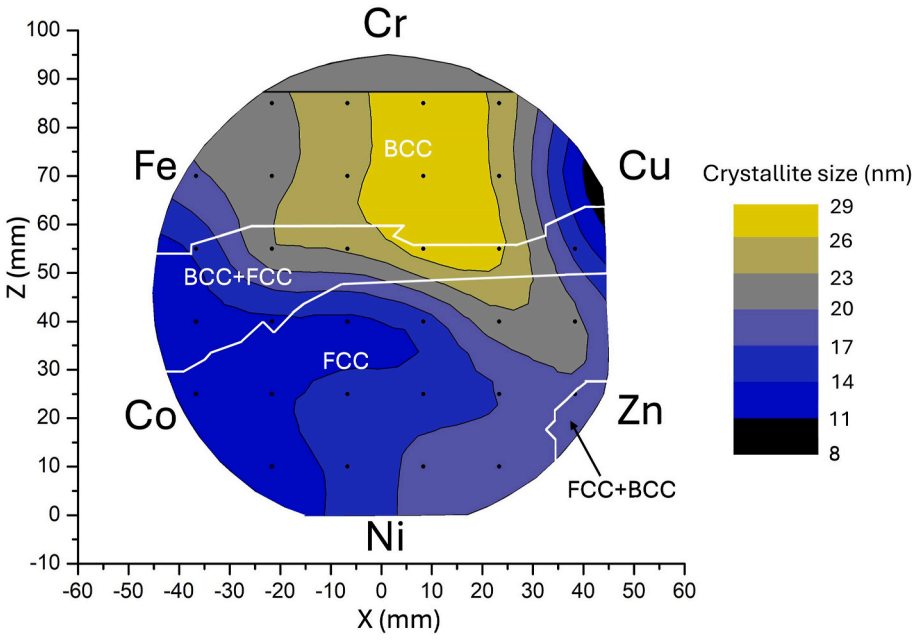

Fig. 7. Map of the crystallite size values obtained by XLPA for the combinatorial Co–Cr–Cu–Fe–Ni–Zn coating.

whole layer (see the right side of Fig. 10a). The width of the pore channels varies between 5 and 40 nm as shown in Fig. 10a and b.

The columns between the pore channels were grown perpendicular to the substrate and have a width of 100–200 nm. However, these columns are fragmented into smaller crystallites with the size between 10 and 15 nm (see Fig. 10b). This value is in a very good agreement with the crystallite size determined by XLPA (15 nm). Inside the crystallites, there are twin faults as shown in the TEM and HRTEM images in Fig. 10c and d, respectively by yellow arrows. Local TEM-EDS gave the following chemical composition of location No. 1: 14%Co–10%Cr–17%Cu–9% Fe–22%Ni–28%Zn (at%) which is in good agreement with the XRF result (see Table S1 in the Supplementary materials). Fig. 11 shows EDS elemental maps of the six constituents and oxygen and a HAADF image corresponding to the studied area. It is evident that between the columns in the coating there are voids and oxygen-rich volumes which are indicated by blue and white arrows, respectively. The surface of the

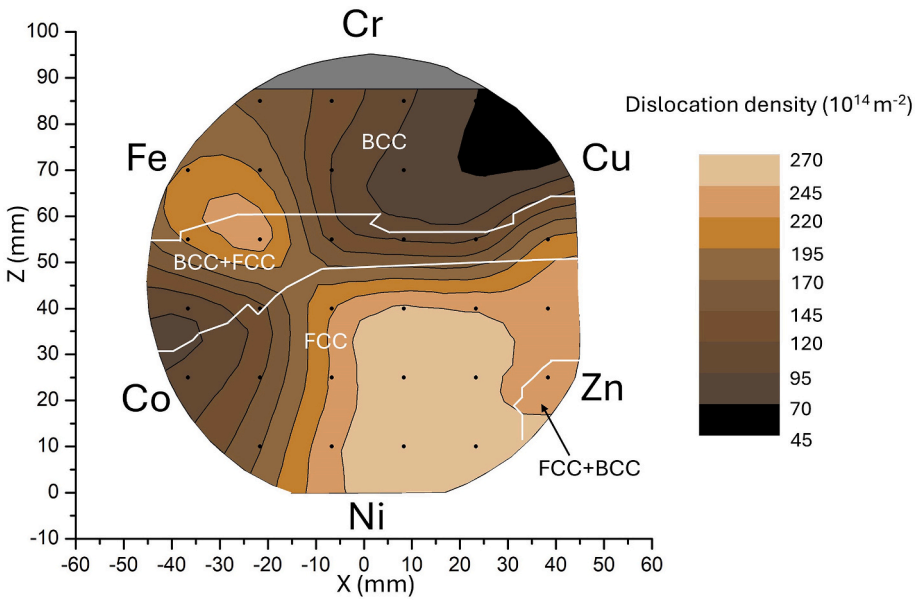

Fig. 8. Map of the dislocation density values determined by XLPA for the combinatorial Co–Cr–Cu–Fe–Ni–Zn coating.

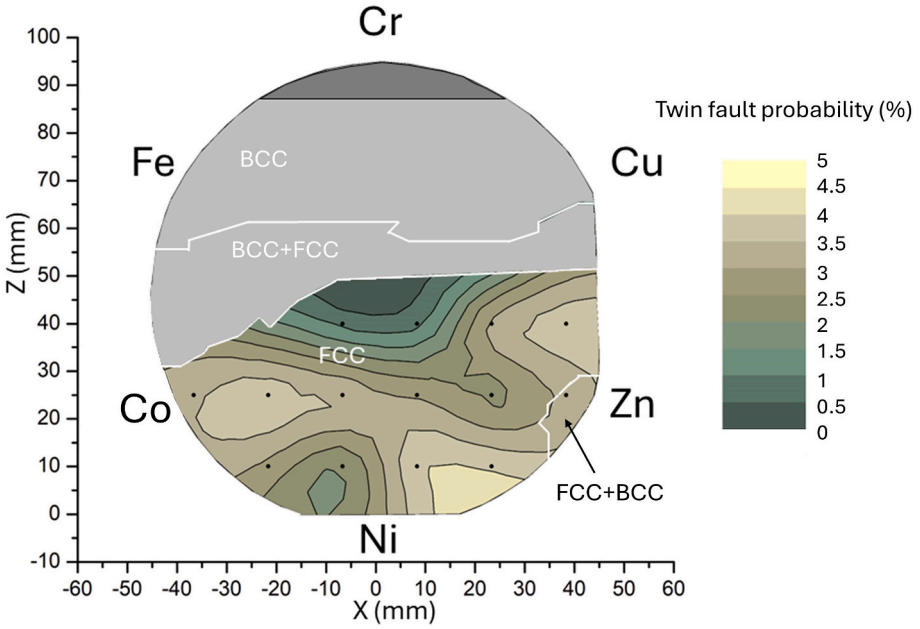

Fig. 9. Map of the twin fault probability in the regions where the major phase is FCC.

voids are also enriched in oxygen as shown in Fig. 11h. In the oxygen-rich material between the columns, the Zn content is also elevated while there is a lack of other elements. Since there are no secondary peaks in the X-ray and TEM diffraction patterns, most probably the material between the columns is an amorphous zinc-oxide. This phase can form after deposition since in the sputtering chamber the partial pressure of the gases containing oxygen was less than 10^{-10} mbar.

Fig. 12 shows the TEM/HRTEM micrographs obtained for location No. 2 which corresponds to the boundary between the single-phase FCC and the two-phase FCC-BCC regions (see the XRD phase map in Fig. 5a). Although, XRD suggested a low amount of BCC secondary phase beside FCC, the TEM diffraction patterns contain only FCC rings. This difference may be caused by the local nature of TEM observations while XRD investigated a much larger volume. Fig. 12a shows that the thickness of the layer is about 2.3 μm. The film consists of columns lying perpendicular to the surface and having a thickness between 100 and 300 nm. The columns contain crystallites with an average size of about 12 nm. This value agrees with the average crystallite size obtained by XLPA. Unlike in the location No. 1, most of the crystallites are not lying parallel to the film normal at point No. 2; rather, they are at an angle of 45° to the layer surface as can be seen in Fig. 12b. In addition, this material has no considerable crystallographic texture as indicated by SAED.

Many columns are separated by pore channels as shown in Fig. 12a and b. The largest pore channels are aligned more or less perpendicular to the surface and have a thickness of about 30 nm. Fig. 12c and d reveal that the crystallites contain twin faults in accordance with the XLPA observation. Fig. 13 shows a HAADF image and the corresponding EDS elemental maps. TEM-EDS gave the following average chemical composition of location No. 2: 25%Co–15%Cr–10%Cu–24%Fe–15%

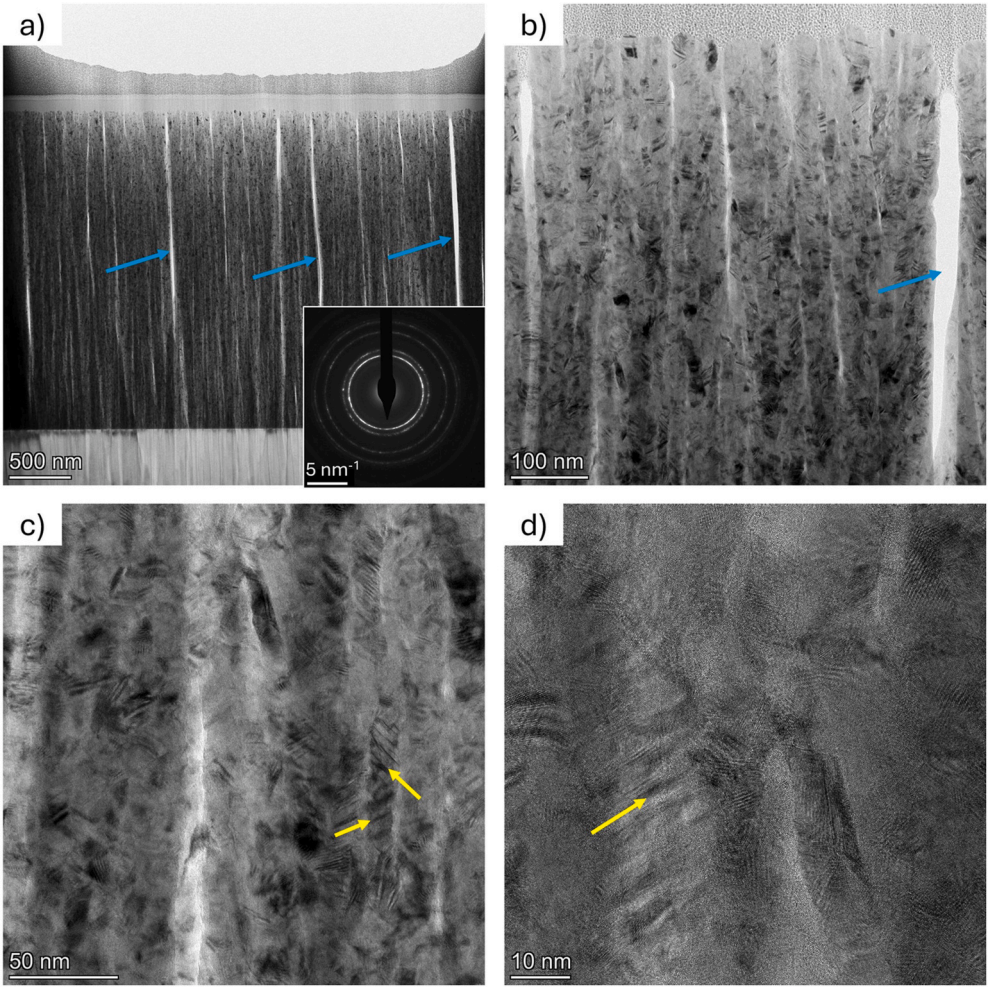

Fig. 10. TEM images taken at the position marked as No. 1 in Fig. 5a a) overview of the coating cross-section, b) magnified image of voids, c) TEM image showing twin faults, d) HRTEM image of twin faults. The inset in (a) shows the corresponding SAED pattern. The blue and the yellow arrows indicate the positions of voids and twin faults, respectively. (For interpretation of the references to colour in this figure legend, the reader is referred to the Web version of this article.)

Ni–11%Zn (at%). This value is in good agreement with the XRF result presented in Table S1 in the Supplementary materials. Compared to point No. 1, this material contains less pores: e.g., in Fig. 13a no pores were detected. On the other hand, the crystallites are separated by oxygen-rich boundaries where the concentrations of Co, Cu, Fe and Ni are lower than inside the crystallites. Significant variation in Cr and Zn contents was not observed at location No. 2.

Fig. 14 shows TEM images taken at position No. 3. This point of investigation can be found in the single-phase BCC region, which has the lowest hardness in the whole combinatorial disk. The reduced hardness can be attributed to the very high porosity of the material at this location, as suggested by the cross-sectional TEM image in Fig. 14a. The columns formed during the film growth have an average width of about 100 nm and are separated by long pore-channels with the width varying between 10 and 40 nm (see Fig. 14a and b). The crystallites building up the columns have a size of about 10–20 nm, which is close to the crystallite size determined by XLPA (~25 nm). The crystallites are at an angle of 45° to the layer surface, as can be seen in Fig. 14b and c. SAED pattern revealed a <110> crystallographic texture in the film. It should be noted that the diffraction pattern taken in TEM contained traces of FCC reflections beside the main BCC peaks. However, this FCC phase has only a very low fraction since its fingerprint was not observed in the X-ray diffractogram. In the boundaries of the columns, besides the voids, a non-crystalline phase was also formed (see Fig. 14c). The EDS elemental maps in Fig. 15 suggest that this amorphous phase is enriched in Zn and oxygen and depleted of Co, Cr, Cu, Fe and Ni. The average chemical composition of the columns at position No. 3 is 7%Co–27%Cr–30% Cu–11%Fe–8%Ni–18%Zn (at%), which agrees with the concentrations determined by XRF technique (see also Table S1 in the Supplementary materials).

Fig. 16 shows TEM images obtained on the cross-section of the combinatorial disk at location No. 4. This point can be found in the single-phase BCC region and has the highest hardness in the whole sample. On the basis of Fig. 16a, the thickness of the layer is about 2.6 μm. It seems that this part of the combinatorial sample contains much less voids than the other locations studied by TEM, and this observation can explain the relatively high hardness at location No. 4. The microstructure contains columns grown perpendicular to the substrate (see Fig. 16a), similar to other studied locations. The width of these columns varies between 100 and 200 nm. It is noted that close to the surface, the columns have a fan-like shape, which is unique compared to other investigated locations. The columns contain crystallites with the size of 10–20 nm (see Fig. 16b and c) which value is in accordance with the results of XLPA. The crystallites are at an angle of 75–90° to the layer surface. SAED indicated that the BCC structure has a <110> texture.

Fig. 17 shows a HAADF micrograph and the corresponding TEM-EDS maps for the constituent elements of the studied MPEA and oxygen at location No. 4. The average chemical composition of the crystallites at this point is 10%Co–38%Cr–13%Cu–27%Fe–5%Ni–7%Zn (at%) which agrees well with the concentrations determined by XRF technique (see

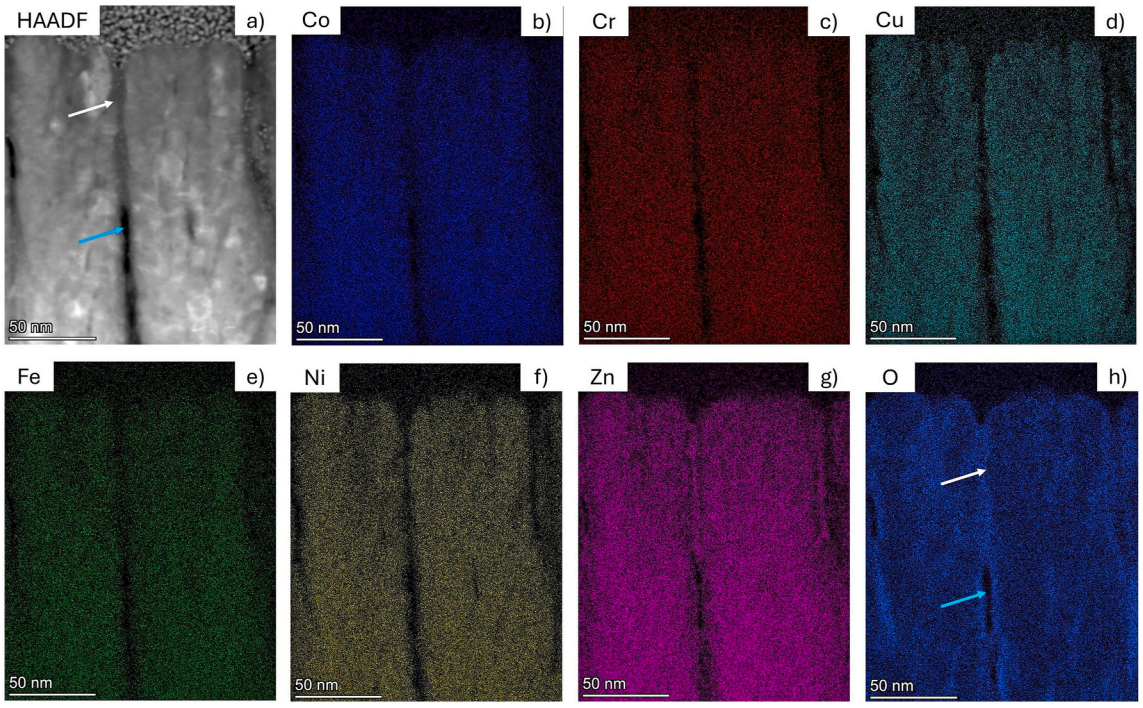

Fig. 11. a) HAADF image taken at the location marked as No. 1 in Fig. 5a. EDS elemental maps for b) Co, c) Cr, d) Cu, e) Fe, f) Ni, g) Zn and h) O. The blue and the white arrows indicate the positions of voids and oxides, respectively. (For interpretation of the references to colour in this figure legend, the reader is referred to the Web version of this article.)

also Table S1 in the Supplementary materials). Fig. 17a revealed that very small pores with the size of about 2 nm developed at the boundaries of the crystallites. In addition, these boundaries are enriched in Zn and oxygen while depleted of Co, Cr, Cu, Fe and Ni as shown in Fig. 17b–h.

4. Discussion

4.1. Compositional dependence of the phase content and the lattice constant

The phase map determined by XRD and shown in Fig. 3 is worth comparing with theoretical predictions. Different theoretical methods have been elaborated for the prediction of the phase content as a function of the chemical composition of MPEAs [31–35]. The most straightforward procedure is based on the valence electron concentration (VEC), which predicts the compositional dependence of the formation of FCC and BCC phases [36]. VEC is obtained as the average of the VEC values of the constituents weighted with their atomic fractions [37]. It was claimed that an FCC phase forms if the VEC value is higher than 8, while the structure is body-centered cubic (BCC) when the VEC is lower than about 7 [37]. If the VEC value is between 7 and 8, the two phases coexist. A revised version of the VEC rule suggests that the BCC phase is stable only if the VEC is lower than 6.87 [38]. For the presently studied MPEA constituents, the VEC has the following values: 9, 6, 11, 8, 10 and 12 for Co, Cr, Cu, Fe, Ni and Zn, respectively. Thus, using the concentrations obtained by XRF on the disk surface for all points in the combinatorial sample, the average VEC varied between 8.1 and 10.5. Therefore, on the basis of the empirical rule existing in the literature, the whole disk should be a single-phase FCC. On the other hand, more than half of the coating is a single-phase BCC or has a dual-phase BCC + FCC structure (see Fig. 3). Most probably, the phases formed during sputtering are not in thermodynamic equilibrium; thus, they do not follow the traditional VEC-based structural prediction. Nevertheless, Fig. 18 shows a map of the VEC values calculated for the presently studied Co–Cr–Cu–Fe–Ni–Zn combinatorial sample. Although, the phase composition does not follow quantitatively the prediction based on the VEC, as discussed above, it is evident that in the FCC region the average VEC value is higher than that for the BCC phase area. This trend agrees qualitatively with the VEC rule which predicts an increase of the stability of the FCC phase with increasing the VEC value [37,38]. It is worth conducting further studies to inspect the change of the phase composition when the targets are placed in other positions around the substrate disk and compare this new phase map with the corresponding VEC values.

In both BCC and FCC phases, the lattice constant increases with increasing the coordinate X as shown in Fig. 4. This effect may be caused by the arrangement of the targets. Namely, Zn target was placed on the right side of the disk and this element has the largest atomic radius among the six target materials (see later). In the disk, closer to each target, the concentration of the target element is enhanced, thus, in the vicinity of the Zn target, the lattice constant is higher. This effect is illustrated in Fig. 19, where the average atomic radius map is plotted. The average atomic radius is determined from the element concentration values determined by XRF and the atomic radii of the constituents. In this calculation, the metallic atomic radii listed in Ref. [39] were used since the constituent elements form metallic alloy in the studied combinatorial material. This type of atomic radius is defined as the half the distance between the centres of the adjacent atoms in a single-component solid body; however, this distance depends on the atomic coordination number. For FCC structure, the metallic atomic radii are 125, 125, 126, 128, 129 and 137 p.m. for Co, Ni, Fe, Cu, Cr and Zn, respectively. In the case of BCC structure, all atomic radii are lower with a factor of 0.97 due to the smaller coordination number compared to the FCC phase (8 instead of 12). In Fig. 19, the average atomic radius in the main phases was plotted; therefore, in the upper and lower regions, the values corresponding to BCC and FCC structures are mapped, respectively. The change in the average atomic radius is in accordance with the measured trend in the lattice constant (see Fig. 4). Thus, it seems that the lattice constant variation in the BCC and FCC phases is controlled mainly by the atomic radii of the constituents.

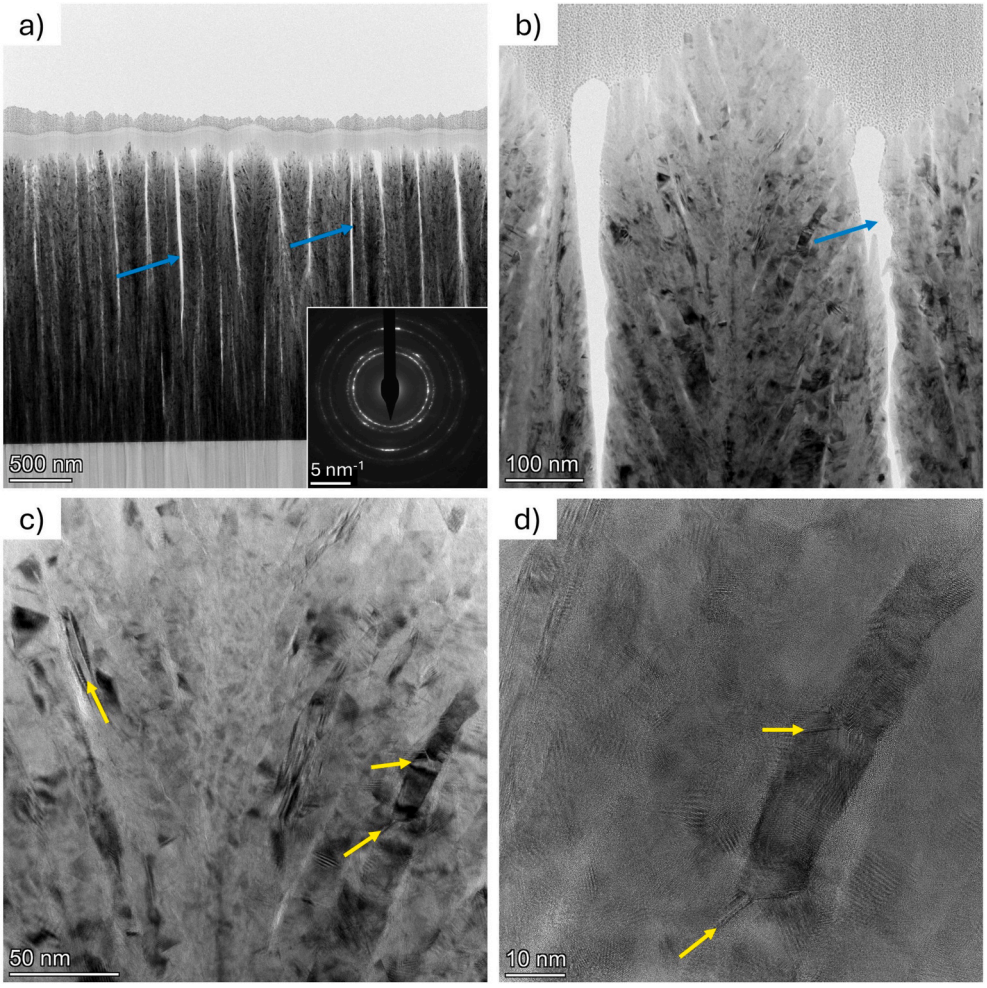

Fig. 12. TEM images taken at the position marked as No. 2 in Fig. 5a a) overview of the coating cross-section, b) magnified image of voids, c) TEM image showing twin faults, d) HRTEM image of twin faults. The inset in (a) shows the corresponding SAED pattern. The blue and the yellow arrows indicate voids and twin faults, respectively. (For interpretation of the references to colour in this figure legend, the reader is referred to the Web version of this article.)

4.2. Correlation between the microstructure and the mechanical behavior

The hardness varied between 1.3 and 3.4 GPa on the presently studied six-component Co–Cr–Cu–Fe–Ni–Zn combinatorial disk. These values are much less than those obtained on the four-component Co–Cr–Fe–Ni combinatorial sample investigated formerly by the same research group [21]. Indeed, in the four-component disk the hardness varied between 8.4 and 11.8 GPa. The much lower hardness in the Co–Cr–Cu–Fe–Ni–Zn combinatorial disk can be attributed to the voids observed in the cross-sectional TEM micrographs. The elastic modulus is also much lower in the six-component Co–Cr–Cu–Fe–Ni–Zn combinatorial specimen (63–119 GPa) than in the four-component Co–Cr–Fe–Ni disk (184–241 GPa) which can also be explained with the porosity of the former sample. In the formerly studied Co–Cr–Fe–Ni disk, significant porosity was not found. In addition, the difference in the phase composition of the two samples (e.g., the formation of the oxide phase in the six-component disk) may also contribute to the different mechanical behaviour.

The highest hardness and elastic modulus were observed in the positions with the chemical composition of 10%Co–38%Cr–13%Cu–27%Fe–5%Ni–7%Zn (location No. 4). This material has a BCC structure and a relatively low porosity (see Fig. 16) which can explain the relatively high hardness compared to other locations in the combinatorial specimen. The lowest hardness and modulus values were determined at location No. 3 with the composition of 7%Co–27%Cr–30%Cu–11%Fe–8%Ni–18%Zn and a relatively high porosity (see Fig. 14). This point can also be found in the single-phase BCC region. In the single-phase FCC area, the porosity variation is less pronounced as suggested by the cross-sectional TEM images (see Figs. 10 and 12). Indeed, the area fractions occupied by the pores in the cross-section of the coatings in points Nos. 1 and 2 are 2.4 and 2.0%, respectively (see Figs. 10a and 12a). These values are much closer than for the two locations studied by TEM in the BCC region. Namely, for points Nos. 3 and 4 the area fractions of voids are 5.2 and 0.5 %, respectively, as obtained from Figs. 14a and 16a. It is worth noting that small pores may be excluded from this evaluation since they overlap with material when electrons transmit through the TEM foil, and therefore, their contrast is reduced in the TEM image. Nevertheless, the highest and lowest porosities in locations Nos. 3 and 4, respectively, are in coincidence with the lowest and highest hardness and elastic modulus values. The moderate variation of porosity in the FCC region is in line with the relatively small change in the elastic modulus since it varies in the range ±10% around 80 GPa. Indeed, the Young's modulus is influenced rather by the chemical and phase composition and the porosity while the hardness depends additionally on the microstructure (e.g., on defect density). In both the FCC and BCC regions, the hardness variation is more pronounced compared to the change of the elastic modulus which can be attributed to the additional effect of the microstructure on the former quantity. For instance, in the FCC area the higher dislocation density values can be found at the right side of the map where the Zn and Ni concentrations are higher (see Fig. 8), and in this part of the combinatorial sample the hardness is also enhanced compared to the left side of the FCC region (see Fig. 5a). In

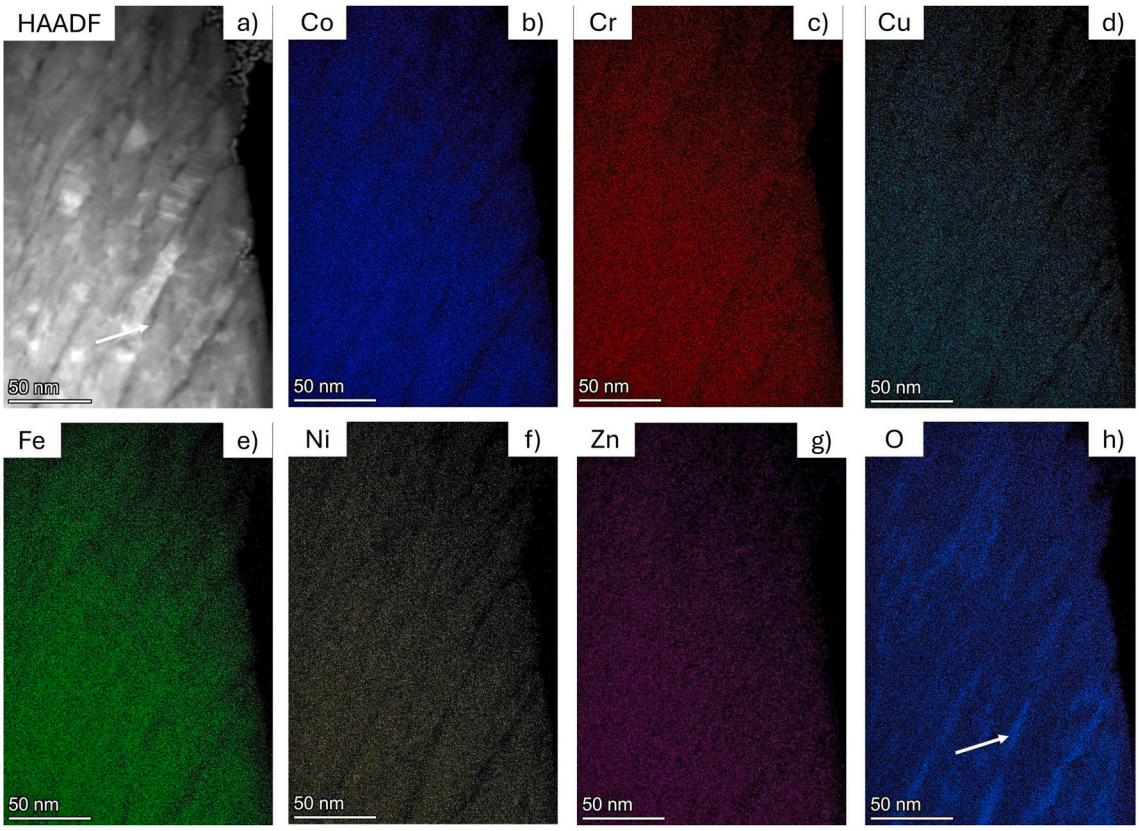

Fig. 13. a) HAADF image taken at the location position marked as No. 2 in Fig. 5a. EDS elemental maps for b) Co, c) Cr, d) Cu, e) Fe, f) Ni, g) Zn and h) O. The white arrow indicates the position of an oxide phase at grain boundaries.

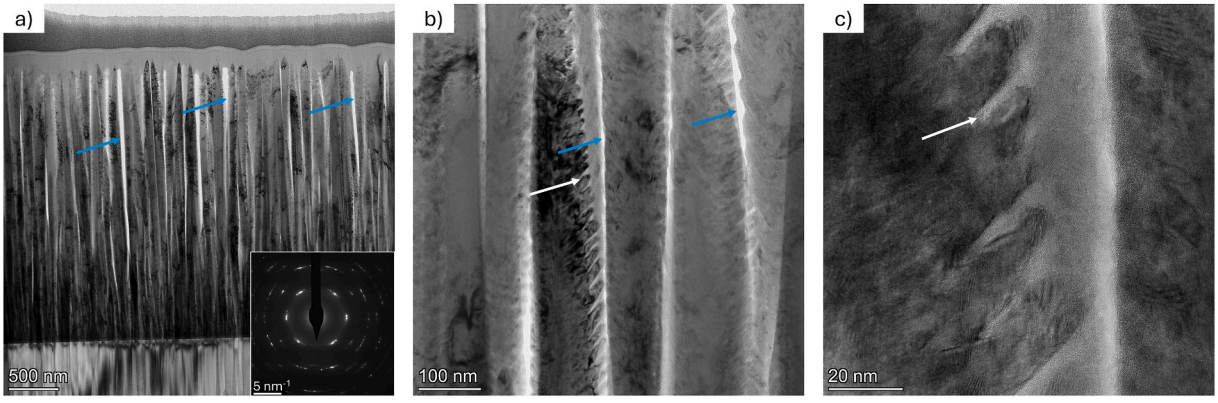

Fig. 14. TEM images taken at position No. 3 in Fig. 5a a) overview of the coating cross-section, b) magnified image of voids, c) TEM image showing oxide phase at grain boundaries. The inset in (a) shows the corresponding SAED pattern. The blue and the white arrows indicate the positions of voids and oxides, respectively, in the boundaries of the columns formed during film growth. (For interpretation of the references to colour in this figure legend, the reader is referred to the Web version of this article.)

addition, the twin fault probability is also high close to the Ni and Zn targets. Nevertheless, a quantitative relationship between the mechanical properties and the microstructure cannot be obtained since the porosity values are not available for the majority of the studied locations.

A further research goal is to produce porosity- and oxide-free combinatorial sample where the correlation between the mechanical properties and the microstructure can be investigated more deeply. For this purpose, an improvement of the sputtering technique is required. The penetration of atmospheric oxygen, and consequent surface oxide formation is morphology and composition dependent. A solution is proposed for improving the morphology of the deposited film. The recent advance of high frequency pulsed DC power sources for magnetron sputtering allows a better tuning of adatom energies via the control of duty cycle, pulse width and pulsing frequency. This approach enables the synthesis of dense coatings with better control of morphology and can prevent the formation of columnar structure, pores and oxide. In this scenario, each magnetron would require an independent power source, and the tuning of their parameter sets by morphology analysis.

5. Conclusions

Experiments were conducted to study the six-component Co–Cr–Cu–Fe–Ni–Zn compositional library. Therefore, a combinatorial

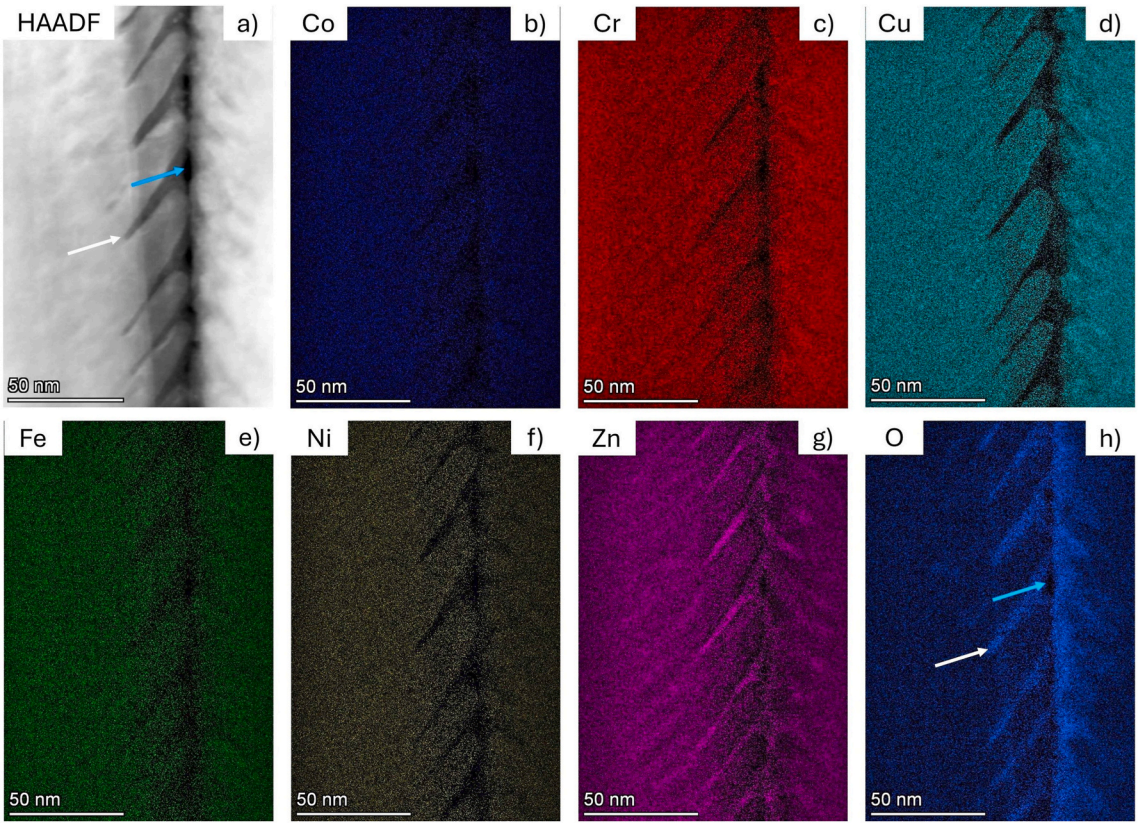

Fig. 15. a) HAADF image taken at the location position marked as No. 3 in Fig. 5a. EDS elemental maps for b) Co, c) Cr, d) Cu, e) Fe, f) Ni, g) Zn and h) O. The blue and the white arrows indicate the positions of voids and oxide phase, respectively. (For interpretation of the references to colour in this figure legend, the reader is referred to the Web version of this article.)

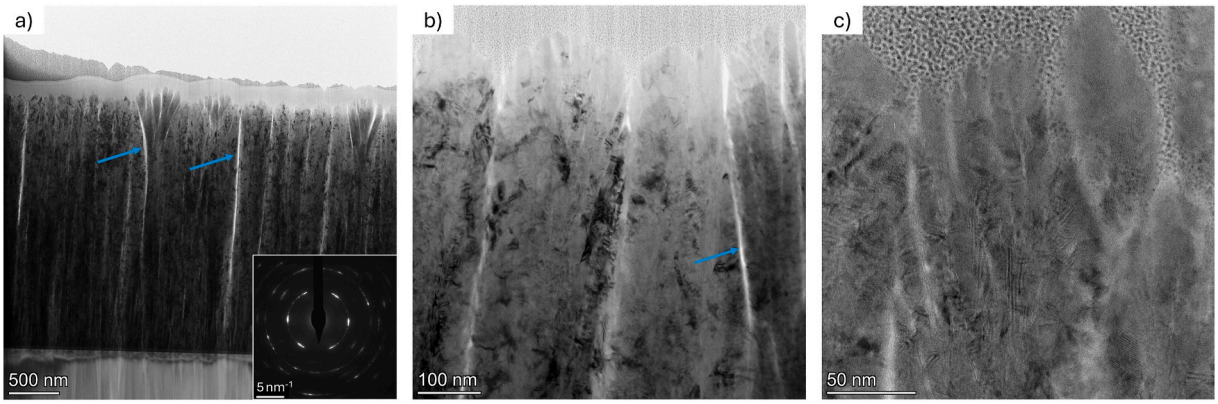

Fig. 16. TEM images taken at the position marked as No. 4 in Fig. 5a a) overview of the coating cross-section, b-c) magnified images showing voids. The inset in (a) shows the corresponding SAED pattern. The blue arrows indicate the positions of voids. (For interpretation of the references to colour in this figure legend, the reader is referred to the Web version of this article.)

high-entropy alloy coating was deposited by the magnetron sputtering technique on a single crystal silicon substrate. The following results were obtained.

1. The layer thickness varied between 1960 and 2830 nm, and the highest value was obtained close to the Zn target. The concentrations of the different elements were in the range of 5–42%. Single-phase FCC and BCC regions, as well as an intermediate two-phase area were identified in the coating. The single-phase FCC and BCC regions formed close to the Fe/Cr/Cu and Co/Ni/Zn targets, respectively. The experimentally observed phase composition does not follow the traditional VEC-based structural prediction which suggests single FCC phase for the whole disk. On the other hand, the VEC rule was held in the sense that in the FCC region the average VEC was higher than in the BCC phase area. The difference between the experimentally observed and the predicted phase contents may be caused by the non-equilibrium nature of the phases formed during sputtering. The change of the lattice constant of the BCC and FCC phases versus the chemical composition was successfully explained by the variation of the average atomic radii of the constituent elements.
2. In the whole combinatorial sample, the microstructure consists of columns growing perpendicular to the coating surface and having a width between 100 and 300 nm. The columns are fragmented into nanocrystals with the size ranging from 10 to 30 nm. These values

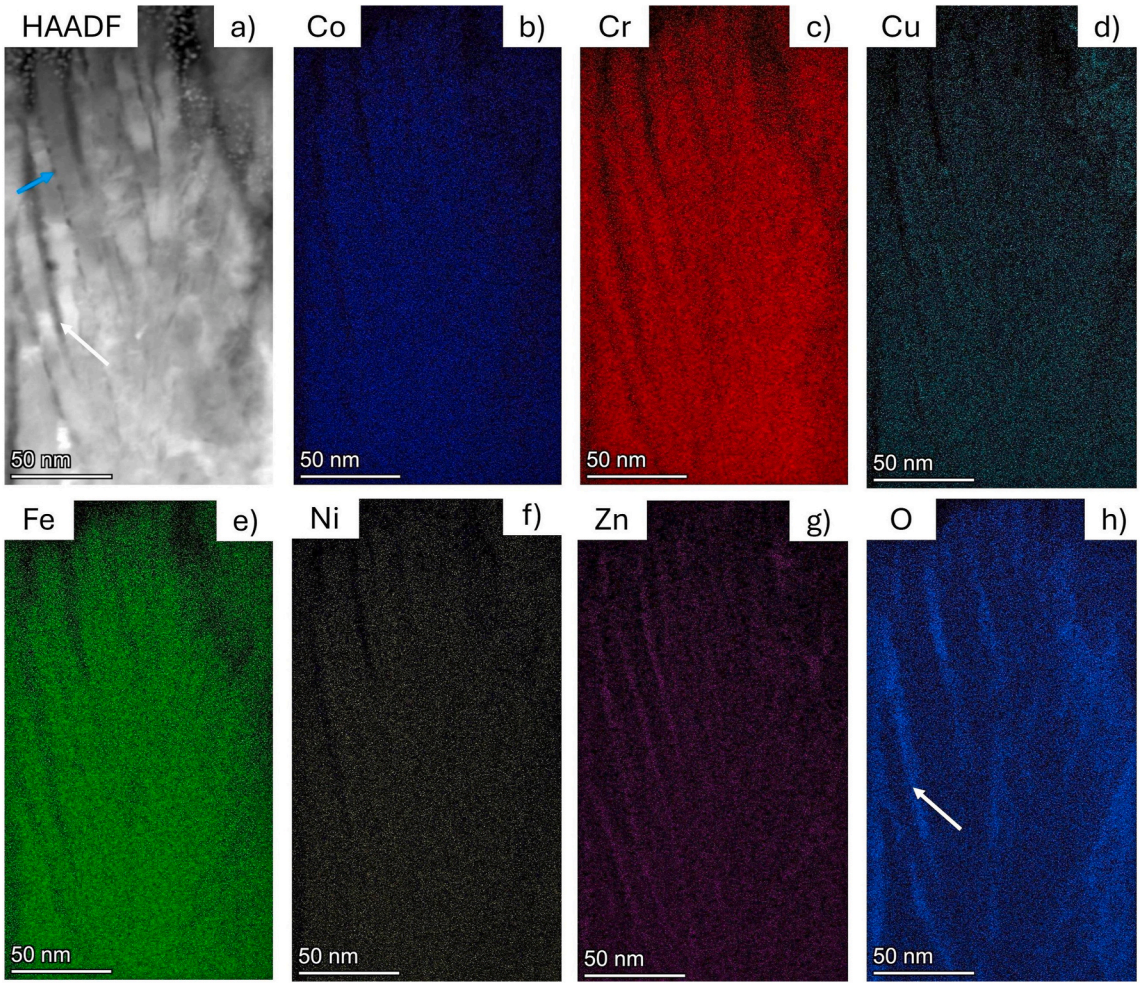

Fig. 17. a) HAADF image taken at the location position marked as No. 4 in Fig. 5a. EDS elemental maps for b) Co, c) Cr, d) Cu, e) Fe, f) Ni, g) Zn and h) O. The blue and the white arrows indicate the positions of voids and oxide phase, respectively. (For interpretation of the references to colour in this figure legend, the reader is referred to the Web version of this article.)

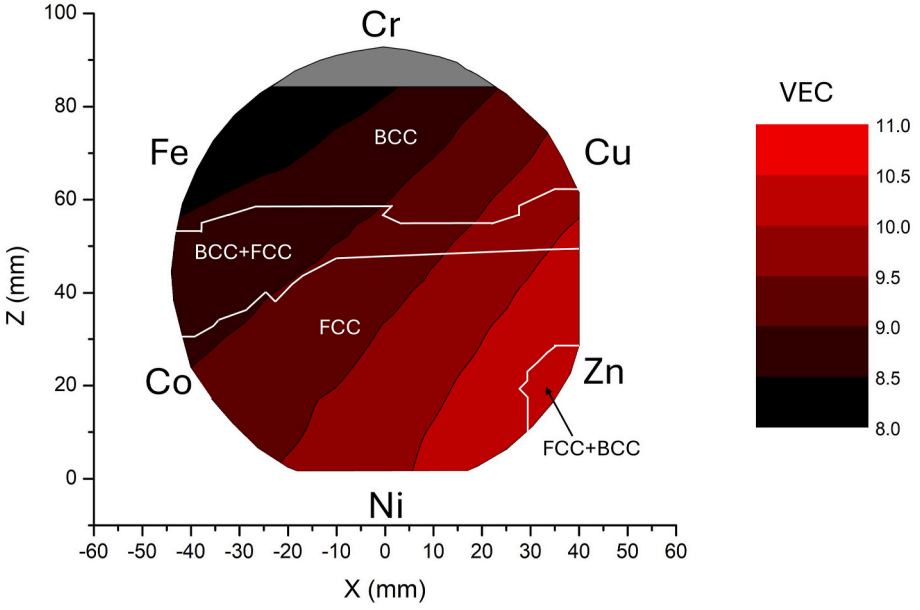

Fig. 18. Map of the VEC values for the studied Co–Cr–Cu–Fe–Ni–Zn combinatorial disk. The white curves indicate the boundaries of the regions with different phase contents.

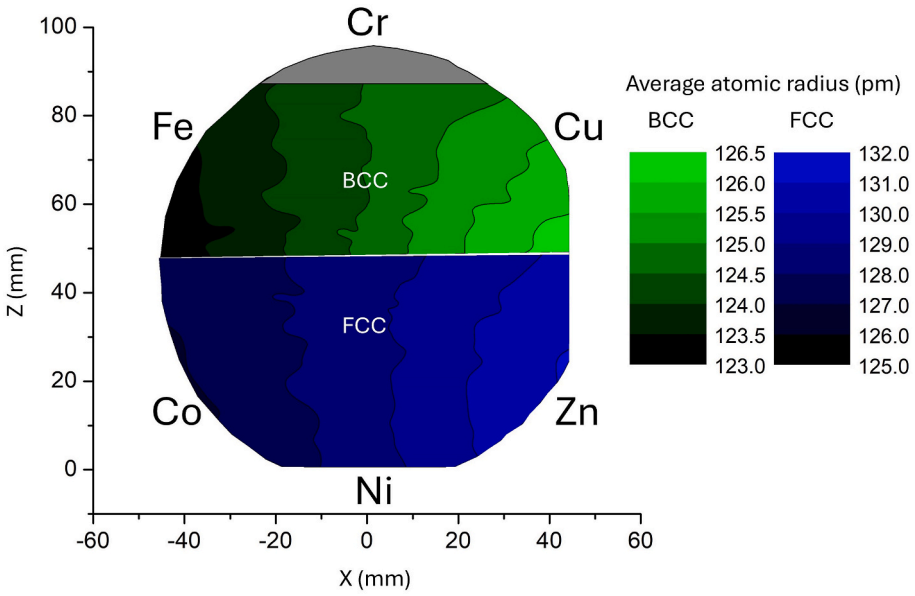

Fig. 19. Map of the average atomic radius for the studied Co–Cr–Cu–Fe–Ni–Zn combinatorial disk. In each location, the atomic radius was calculated for the primary phase. For the two-phase regions identified in Fig. 3, only the average atomic radius of the primary phase is shown in this map. Above and below the horizontal line, the BCC and FCC structures, respectively, are the main phases.

are in a good agreement with the crystallite sizes determined from synchrotron XRD patterns using XLPA method. Between the columns there are long pore channels with the width of about 10–40 nm, but between the nanocrystals very small pores with the size of 2–5 nm were also found. The dislocation density values in the BCC and FCC areas vary between 70 and 190 $\times 10^{14}$ m^{-2} and 110-270 $\times 10^{14}$ m^{-2}, respectively. The twin fault probability values varied between 0.4 and 4.3% in the FCC region. The highest defect density values were detected close to the coating perimeter between the Ni and Zn targets.

3. The hardness and the elastic modulus varied in the ranges of 1.3–3.4 and 63–119 GPa, respectively. These values are much less than those obtained on a four-component Co–Cr–Fe–Ni combinatorial sample investigated formerly which can be attributed to the porosity in the six-component layer. Indeed, the lowest and highest hardness and modulus were measured in the locations where the porosity values were the largest and smallest, respectively. These two points were located in the BCC region with the compositions of 7%Co–27% Cr–30%Cu–11%Fe–8%Ni–18%Zn (lowest hardness) and 10% Co–38%Cr–13%Cu–27%Fe–5%Ni–7%Zn (highest hardness). In the FCC area, the higher hardness values were measured in the points where the Zn and Ni concentrations are higher, and this trend can be attributed to the elevated defect density.

Data availability

Data will be made available on request.

Declaration of competing interest

The authors declare that they have no known competing financial interests or personal relationships that could have appeared to influence the work reported in this paper.

Acknowledgements

This research was supported by the grant no. VEKOP-2.3.3-15-2016-00002 and VEKOP-2.3.2-16-2016-00011 of the European Structural and Investment Funds. We acknowledge DESY (Hamburg, Germany), a member of the Helmholtz Association HGF, for the provision of experimental facilities. Parts of this research were carried out at beamline P21.2.

Appendix ASupplementary data

Supplementary data to this article can be found online at https://doi.org/10.1016/j.jmrt.2024.06.059.

References

[1] Cantor B, Chang ITH, Knight P, Vincent AJB. Microstructural development in equiatomic multicomponent alloys. Mater Sci Eng 2004;375–377:213–8. https://doi.org/10.1016/j.msea.2003.10.257.
[2] Yeh JW, Chen SK, Lin SJ, Gan JY, Chin TS, Shun TT, Tsau CH, Chang SY. Nanostructured high-entropy alloys with multiple principal elements: novel alloy design concepts and outcomes. Adv Eng Mater 2004;6:299–303. https://doi.org/10.1002/adem.200300567.
[3] Yeh JW. Alloy design strategies and future trends in high-entropy alloys. JOM 2013;65:1759–71. https://doi.org/10.1007/s11837-013-0761-6.
[4] Li W, Liu P, Liaw PK. Microstructures and properties of high-entropy alloy films and coatings: a review. Mater Res Lett 2018;6:199–229. https://doi.org/10.1080/21663831.2018.1434248.
[5] Huo W, Liu X, Tan S, Fang F, Xie Z, Shang J, Jiang J. Ultrahigh hardness and high electrical resistivity in nano-twinned, nanocrystalline high-entropy alloy films. Appl Surf Sci 2018;439:222–5. https://doi.org/10.1016/j.apsusc.2018.01.050.
[6] Qiu Y, Thomas S, Fabijanic D, Barlow AJ, Fraser HL, Birbilis N. Microstructural evolution, electrochemical and corrosion properties of Al x CoCrFeNiTi y high entropy alloys. Mater Des 2019;170:107698. https://doi.org/10.1016/j.matdes.2019.107698.
[7] Cui K, Zhang Y. High-entropy alloy films. Coatings 2023;13:635. https://doi.org/10.3390/coatings13030635.
[8] Senkov ON, Scott JM, Senkova SV, Meisenkothen F, Miracle DB, Woodward CF. Microstructure and elevated temperature properties of a refractory TaNbHfZrTi alloy. J Mater Sci 2012;47:4062–74. https://doi.org/10.1007/s10853-012-6260-2.
[9] Kim YS, Park HJ, Mun SC, Jumaev E, Hong SH, Song G, Kim JT, Park YK, Kim KS, Jeong SI, Jeong SI, Kwon YH, Kim KB. Investigation of structure and mechanical properties of TiZrHfNiCuCo high entropy alloy thin films synthesized by magnetron sputtering. J Alloys Compd 2019;797:834–41. https://doi.org/10.1016/j.jallcom.2019.05.043.
[10] Haciismailoglu MC, Sarlar K, Tekgül A, Kucuk I. Thermally evaporated FeMGaMnSi (M[dbnd]Co, Ni) high entropy alloy thin films: magnetic and magnetoresistance properties. J Non-Cryst Solids 2020;539:120063. https://doi.org/10.1016/j.jnoncrysol.2020.120063.
[11] Özbilen S, Vasquez JFB, Abbott WM, Yin S, Morris M, Lupoi R. Mechanical milling/alloying, characterization and phase formation prediction of Al0.1–0.5(Mn) CoCrCuFeNi-HEA powder feedstocks for cold spray deposition processing. J Alloys Compd 2023;961:170854. https://doi.org/10.1016/J.JALLCOM.2023.170854.
[12] Khan NA, Akhavan B, Zhou C, Zhou H, Chang L, Wang Y, Liu Y, Fu L, Bilek MM, Liu Z. RF magnetron sputtered AlCoCrCu0.5FeNi high entropy alloy (HEA) thin

films with tuned microstructure and chemical composition. J Alloys Compd 2020; 836:155348. https://doi.org/10.1016/j.jallcom.2020.155348.
[13] Nagy P, Rohbeck N, Roussely G, Sortais P, Lábár JL, Gubicza J, Michler J, Pethö L. Processing and characterization of a multibeam sputtered nanocrystalline CoCrFeNi high-entropy alloy film. Surf Coat Technology 2020;386:125465. https://doi.org/10.1016/j.surfcoat.2020.125465.
[14] Dolique V, Thomann AL, Brault P, Tessier Y, Gillon P. Thermal stability of AlCoCrCuFeNi high entropy alloy thin films studied by in-situ XRD analysis. Surf Coat Technol 2010;204:1989–92. https://doi.org/10.1016/j.surfcoat.2009.12.006.
[15] Gubicza J. Combinatorial design of novel multiprincipal element alloys using experimental techniques. Adv Eng Mater 2023;26:6. https://doi.org/10.1002/adem.202301673.
[16] Nagy P, Kaszás B, Csabai I, Hegedűs Z, Michler J, Pethö L, Gubicza J. Machine learning-based characterization of the nanostructure in a combinatorial Co-Cr-Fe-Ni compositionally complex alloy film. Nanomaterials 2022;12:4407. https://doi.org/10.3390/nano12244407.
[17] Yang J, Wang C, Xie D, Qin H, Liu W, Liang M, Li X, Liu C, Huang M. A new type of gradient structure FeCoCrNiWMo high entropy alloy layer by plasma solid-state surface metallurgy. Surf Coat Technol 2023;457:129320. https://doi.org/10.1016/J.SURFCOAT.2023.129320.
[18] Schweidler S, Schopmans H, Reiser P, Boltynjuk E, Olaya JJ, Singaraju SA, Fischer F, Hahn H, Friederich P, Velasco L. Synthesis and characterization of high-entropy CrMoNbTaVW thin films using high-throughput methods. Adv Eng Mater 2023;25:2. https://doi.org/10.1002/adem.202200870.
[19] Marshal A, Pradeep KG, Music D, Wang L, Petracic O, Schneider JM. Combinatorial evaluation of phase formation and magnetic properties of FeMnCoCrAl high entropy alloy thin film library. Sci Rep 2019;9:7864. https://doi.org/10.1038/s41598-019-44351-8.
[20] Nagy P, Rohbeck N, Hegedűs Z, Michler J, Pethö L, Lábár JL, Gubicza J. Microstructure, hardness, and elastic modulus of a multibeam-sputtered nanocrystalline Co-Cr-Fe-Ni compositional complex alloy film. Materials 2021;14:3357. https://doi.org/10.3390/ma14123357.
[21] Nagy P, Rohbeck N, Widmer RN, Hegedűs Z, Michler J, Pethö L, Lábár JL, Gubicza J. Combinatorial Study of Phase Composition, Microstructure and Mechanical Behavior of Co-Cr-Fe-Ni Nanocrystalline Film Processed by Multiple-Beam-Sputtering Physical Vapor Deposition 2022;15(6):2319. https://doi.org/10.3390/ma15062319.
[22] Kauffmann A, Stüber M, Leiste H, Ulrich S, Schlabach S, Szabó DV, Seils S, Gorr B, Chen H, Seifert HJ, Heilmaier M. Combinatorial exploration of the high entropy alloy system Co-Cr-Fe-Mn-Ni. Surf Coat Technol 2017;325:25. https://doi.org/10.1016/j.surfcoat.2017.06.041.
[23] Nene SS, Frank M, Liu K, Sinha S, Mishra RS, McWilliams BA, Cho KC. Corrosion-resistant high entropy alloy with high strength and ductility. Scr Mater 2019;166:168–72. https://doi.org/10.1016/J.SCRIPTAMAT.2019.03.028.
[24] Sharma A, Lee H, Ahn B. Effect of additive elements (x = Cr, Mn, Zn, Sn) on the phase evolution and thermodynamic complexity of AlCuSiFe-x high entropy alloys fabricated via powder metallurgy. Met Mater Int 2022;28:2216–24. https://doi.org/10.1007/s12540-021-01125-0.
[25] Sharma A, Lee H, Ahn B. Tailoring compressive strength and absorption energy of lightweight multi-phase alcusifex (X = cr, mn, zn, sn) high-entropy alloys processed via powder metallurgy. Materials 2021;14:4945. https://doi.org/10.3390/ma14174945.
[26] Gubicza J. X-ray line profile analysis in materials science. Hershey, PA: IGI Global 2014. https://doi.org/10.4018/978-1-4666-5852-3.
[27] Ribárik G, Gubicza J, Ungár T. Correlation between strength and microstructure of ball-milled Al-Mg alloys determined by X-ray diffraction. Mater Sci Eng 2004; 387–389:343–7. https://doi.org/10.1016/j.msea.2004.01.089.
[28] Gubicza J, Hung PT, Kawasaki M, Han JK, Zhao Y, Xue Y, Lábár JL. Influence of severe plastic deformation on the microstructure and hardness of a CoCrFeNi high-entropy alloy: a comparison with CoCrFeNiMn. Mater Char 2019;154:304–14. https://doi.org/10.1016/j.matchar.2019.06.015.
[29] Nelson JB, Riley DP. An experimental investigation of extrapolation methods in the derivation of accurate unit-cell dimensions of crystals. Proc Phys Soc 1945;57:160. https://doi.org/10.1088/0959-5309/57/3/302.
[30] Oliver WC, Pharr GM. An improved technique for determining hardness and elastic modulus using load and displacement sensing indentation experiments. J Mater Res 1992;7:1564–83. https://doi.org/10.1557/jmr.1992.1564.
[31] Wang S, Xiong J, Li D, Zeng Q, Xiong M, Chai X. Comparison of two calculation models for high entropy alloys: virtual crystal approximation and special quasi-random structure. Mater Lett 2021;282:128754. https://doi.org/10.1016/J.MATLET.2020.128754.
[32] Zhang L, Qian K, Huang J, Liu M, Shibuta Y. Molecular dynamics simulation and machine learning of mechanical response in non-equiatomic FeCrNiCoMn high-entropy alloy. J Mater Res Technol 2021;13:2043–54. https://doi.org/10.1016/J.JMRT.2021.06.021.
[33] Conway PLJ, Klaver TPC, Steggo J, Ghassemali E. High entropy alloys towards industrial applications: high-throughput screening and experimental investigation. Mater Sci Eng, A 2022;830:142297. https://doi.org/10.1016/J.MSEA.2021.142297.
[34] Wu Q, Wang Z, Hu X, Zheng T, Yang Z, He F, Li J, Wang J. Uncovering the eutectics design by machine learning in the Al–Co–Cr–Fe–Ni high entropy system. Acta Mater 2020;182:278–86. https://doi.org/10.1016/J.ACTAMAT.2019.10.043.
[35] Huang W, Martin P, Zhuang HL. Machine-learning phase prediction of high-entropy alloys. Acta Mater 2019;169:225–36. https://doi.org/10.1016/J.ACTAMAT.2019.03.012.
[36] Li M, Gazquez J, Borisevich A, Mishra R, Flores KM. Evaluation of microstructure and mechanical property variations in AlxCoCrFeNi high entropy alloys produced by a high-throughput laser deposition method. Intermetallics 2018;95:110–8. https://doi.org/10.1016/J.INTERMET.2018.01.021.
[37] Yang S, Lu J, Xing F, Zhang L, Zhong Y. Revisit the VEC rule in high entropy alloys (HEAs) with high-throughput CALPHAD approach and its applications for material design-A case study with Al–Co–Cr–Fe–Ni system. Acta Mater 2020;192:11–9. https://doi.org/10.1016/J.ACTAMAT.2020.03.039.
[38] Yang S, Liu G, Zhong Y. Revisit the VEC criterion in high entropy alloys (HEAs) with high-throughput ab initio calculations: a case study with Al-Co-Cr-Fe-Ni system. J Alloys Compd 2022;916:165477. https://doi.org/10.1016/J.JALLCOM.2022.165477.
[39] Weller M, Overton T, Rourke J, Armstrong F. Inorganic chemistry. seventh ed. Oxford, UK: Oxford University Press; 2018.